

Metasurface-generated complex 3-dimensional optical fields for interference lithography

Seyedeh Mahsa Kamali^{a,b,c,d}, Ehsan Arbabi^{a,b}, Hyoungnan Kwon^{a,b}, and Andrei Faraon^{a,b,1}

^aT. J. Watson Laboratory of Applied Physics, California Institute of Technology, Pasadena, CA 91125; ^bKavli Nanoscience Institute, California Institute of Technology, Pasadena, CA 91125; ^cDepartment of Electrical Engineering and Computer Sciences, University of California, Berkeley, CA 94720; and ^dDepartment of Bioengineering, University of California, Berkeley, CA 94720

Edited by Naomi J. Halas, Rice University, Houston, TX, and approved September 18, 2019 (received for review May 15, 2019)

Fast, large-scale, and robust 3-dimensional (3D) fabrication techniques for patterning a variety of structures with submicrometer resolution are important in many areas of science and technology such as photonics, electronics, and mechanics with a wide range of applications from tissue engineering to nanoarchitected materials. From several promising 3D manufacturing techniques for realizing different classes of structures suitable for various applications, interference lithography with diffractive masks stands out for its potential to fabricate complex structures at fast speeds. However, the interference lithography masks demonstrated generally suffer from limitations in terms of the patterns that can be generated. To overcome some of these limitations, here we propose the metasurface-mask-assisted 3D nanofabrication which provides great freedom in patterning various periodic structures. To showcase the versatility of this platform, we design metasurface masks that generate exotic periodic lattices like gyroid, rotated cubic, and diamond structures. As a proof of concept, we experimentally demonstrate a diffractive element that can generate the diamond lattice.

metasurface | 3D printing | interference lithography | beam shaping | nanophotonics

In the 20th century, nanofabrication techniques have truly revolutionized the electronics and photonics industries. As the trend continues, currently there is high interest in fast fabrication of large-scale 3-dimensional (3D) lattices with nanoscale resolution. These structures have applications in various areas including novel engineered materials (1), microelectromechanical systems (2), nanoarchitected materials (3, 4), microelectronics (5), tissue engineering and biomedical engineering (6), micro-fuel cell development (7), optics (8), and micro- and nanofluidics (9). Different 3D manufacturing techniques have been proposed for different applications, including approaches based on self-assembly methods (10, 11), holographic lithography (5, 12–16), multiple-exposures lithography (17), controlled chemical etching (18), and various additive manufacturing methods (19) like stereolithography (20) and laser- or ink-based direct writing (21) among many others. Each of these techniques provides new capabilities for fabricating different classes of 3D structures for different applications beyond traditional 2D photolithography steppers. Nevertheless, none could reach the performance of traditional steppers in simultaneously providing a high-speed, large-scale and scalable lithography, a simple and robust experimental setup, high yield, and defect-free structures. Here, we introduce the concept of large-scale metasurface-assisted 3D lithography, schematically shown in Fig. 1, to circumvent some of these shortcomings. The method is based on using metasurfaces as photolithography masks to generate exotic 3D structures and also take advantage of the traditional stepper technique in fabricating fast, large-scale, 3D patterns with nanometer resolution through a relatively simple and robust process. The metasurface mask (which we call metamask from here on) provides control over the complex coefficients of 2 orthogonal polarizations for various diffraction orders, resulting in the realization of exotic 3D patterns like the

gyroid, diamond, or cubic. As a proof of concept, we experimentally demonstrate the diamond pattern through design and fabrication of a metamask. We should note that conformal masks have been used before for fabricating 3D patterns in photoresists (22, 23). However, they suffer from limited diffraction efficiencies (which result in low-contrast 3D structures) and have limited degrees of freedom in generating desired 3D patterns.

Optical metasurfaces are 2D arrangements of scatterers that are designed to modify different characteristics of light such as its wavefront, polarization, intensity distribution, or spectrum with subwavelength resolution (24–28). By proper design of the scatterers, different characteristics of the incident light can be engineered, and therefore different optical elements like gratings, lenses, holograms, waveplates, polarizers, and spectral filters can be realized (29–37). Furthermore, a single metasurface can provide novel functionalities, which, if at all possible, would require a combination of complex optical elements to implement (38–43). Here, we demonstrate that by exploiting the metasurface capabilities in modifying the phase, intensity, and polarization of the optical wavefront, different metamasks can be designed to generate 3D patterns like the gyroid, cubic, or diamond structures.

Fig. 24 schematically shows a metamask and how it generates different diffraction orders that interfere to realize a specific

Significance

Fast submicrometer-scale 3D printing techniques are of interest for various applications ranging from photonics and electronics to tissue engineering. Interference lithography is a versatile 3D printing method with the ability to generate complicated nanoscale structures. Its application, however, has been hindered by either the complicated setups in multi-beam lithography that cause sensitivity and impede scalability or the limited level of control over the fabricated structure achievable with mask-assisted processes. Here, we show that metasurface masks can generate complex volumetric intensity distributions with submicrometer scales for fast and scalable 3D printing. These results push the limits of optical devices in controlling the light intensity distribution and significantly increase the realm of possibilities for 3D printing.

Author contributions: S.M.K. and A.F. designed research; S.M.K., E.A., and H.K. performed research; S.M.K. contributed new reagents/analytic tools; S.M.K. and E.A. analyzed data; and S.M.K., E.A., and A.F. wrote the paper.

Competing interest statement: S.M.K., E.A., and A.F. are inventors of US patent application US20190173191A1 that covers the use of metasurface masks for 3D beam shaping. The authors declare no other competing interests.

This article is a PNAS Direct Submission.

This open access article is distributed under [Creative Commons Attribution-NonCommercial-NoDerivatives License 4.0 \(CC BY-NC-ND\)](https://creativecommons.org/licenses/by-nc-nd/4.0/).

¹To whom correspondence may be addressed. Email: faraon@caltech.edu.

This article contains supporting information online at www.pnas.org/lookup/suppl/doi:10.1073/pnas.1908382116/-DCSupplemental.

First published October 7, 2019.

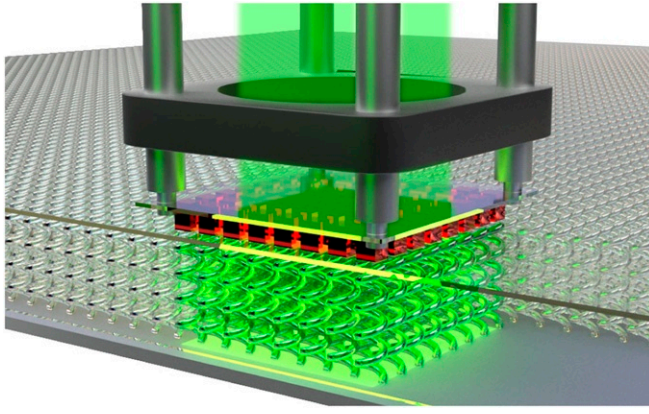


Fig. 1. Concept of large-scale metamask-assisted 3D fabrication. Shown is a schematic illustration of large-scale metasurface-assisted 3D printing. A large metamask ($\sim 1 \text{ cm}^2$) is designed and used as a photolithography mask to create the desired 3D pattern in the photoresist. The large ($\sim 1 \text{ cm}^2$ wide and $\sim 10 \text{ }\mu\text{m}$ thick) 3D pattern is generated inside the photoresist through single-photon lithography. Similar to a stepper, a linear stage could be used here to create large-scale 3D periodic patterns. The rendering just serves to demonstrate the concept and the sizes are not to scale.

desired intensity pattern inside a transparent photoresist. It was previously shown that all 14 Bravais lattices can be formed by interference of 4 noncoplanar beams (44). Therefore, the metamask is in principle capable of generating all Bravais lattices in the resist. In Fig. 2, the illumination is assumed to be a 532-nm laser with linear polarization. The photoresist is assumed to be a sensitized SU-8, with the ability to form a solid structure under 532-nm photoexposure (13, 22, 45). The metamask is assumed to provide the desired amplitude and phase masks for the x - and y -polarized incident light.

The metamask generates different plane waves (diffraction orders) with different propagation directions that are determined by its lateral periods. The electric field associated with the n th plane wave can be written as $\vec{E}_n e^{-j\vec{k}_n \cdot \vec{r}}$. The overall electric field resulting from the interference of these plane waves can be written as

$$\vec{E} = E_x \vec{x} + E_y \vec{y} + E_z \vec{z}, \quad [1]$$

where

$$\begin{aligned} E_x &= \sum_{n=1}^N E_{nx} e^{-j\vec{k}_n \cdot \vec{r}} \\ E_y &= \sum_{n=1}^N E_{ny} e^{-j\vec{k}_n \cdot \vec{r}} \\ E_z &= \sum_{n=1}^N \left(\frac{-\vec{k}_n \cdot \vec{x}}{\vec{k}_n \cdot \vec{z}} E_{nx} e^{-j\vec{k}_n \cdot \vec{r}} + \frac{-\vec{k}_n \cdot \vec{y}}{\vec{k}_n \cdot \vec{z}} E_{ny} e^{-j\vec{k}_n \cdot \vec{r}} \right). \end{aligned} \quad [2]$$

The 3D intensity profile is defined as

$$I = \frac{1}{2\eta} |\vec{E}|^2, \quad [3]$$

where $\eta = \sqrt{\mu/\epsilon}$ is the characteristic impedance of the propagating medium. In single-photon lithography the photoresist polymerization is proportional to the exposure intensity, and therefore the 3D structure is generally formed for intensities above a specific threshold value, defined here as I_{th} .

The main advantage of using metamasks is that the complex coefficients of different x - and y -polarized diffraction orders (E_{nx} and E_{ny}) can be controlled independently and at will. Therefore, it provides more degrees of freedom to define more exotic 3D structures like the gyroid and diamond patterns.

The design process of the metamask to generate a specific 3D periodic lattice is as follows: First, the lateral periods of the 3D structure must be properly selected such that the intensity interference pattern is fully periodic in all 3 dimensions. These lateral dimensions play a critical role as they define the number of diffraction orders and their directions, as well as the in-depth periodicity. After selecting the appropriate lattice constants, the corresponding diffraction order coefficients are optimized to generate the desired 3D pattern. Finally, the metamask is designed and implemented through a high-contrast dielectric transmittarray. To showcase the capability of metamasks, we demonstrate metamasks that generate different lattices like the gyroid, cubic, and diamond patterns. The in-plane dimensions and the corresponding in-depth periods are noted for these structures in *SI Appendix, Fig. S1*.

The level-set representation of the 3 structures is given in *SI Appendix*, in the form of $f(x, y, z) - t > 0$. In these equations, the parameter t is used to control the volume fraction of the structure, as it is assumed to be solid for $f(x, y, z) - t > 0$. This parameter can be controlled experimentally by adjusting the exposure threshold of the photoresist. Here, we have assumed it to be 0.25, 0.15, and 0.3 for defining the gyroid, rotated cubic, and diamond patterns, respectively. See *SI Appendix, Fig. S2* for the defined target patterns. For realizing the patterns with amplitude and phase masks, we used a global optimization technique to find the complex coefficients of different diffraction orders, E_{nx} and E_{ny} , which are given in *SI Appendix, Fig. S2*. The optimized amplitude and phase masks for each pattern, shown in Fig. 2 *B–D, Left*, are calculated from the optimized diffraction order coefficients using Eq. 2 at $z = 0$ plane. The 3D intensity patterns are then calculated using Eq. 2 and are shown in Fig. 2 *B–D, Center*. The corresponding 3D structures, assuming $I_{th} = 0.5$, are shown in Fig. 2 *B–D, Right*. To determine the degree of similarity between the achieved and desired patterns, we used a fitness factor (FF) defined as the fraction of voxels in 1 unit cell that match the 3D target structure. The fitness factors for the gyroid, rotated cubic, and diamond patterns are 97%, 82%, and 93%, respectively (see *Materials and Methods* for simulation details). It is worth noting that the gyroid lattice discussed here is an example of a chiral structure, showing the capability of the developed technique in generation of such chiral patterns (46). Other chiral structures with interesting optical properties [such as spiral lattices (47)] can also be designed using this platform as shown in *SI Appendix, Fig. S6*.

To realize the diamond metamask for 532-nm wavelength, we used a metasurface platform composed of cuboid-shaped crystalline silicon (cSi) nanoposts embedded in an SU-8 protecting layer and resting on a quartz substrate. A schematic of the metasurface platform is shown in Fig. 3A. Transmission phases of the x - and y -polarized light can be fully and independently controlled from 0 to 2π by changing the in-plane dimensions of the nanoposts (39). The cSi nanoposts are 291 nm tall and fully embedded in the SU-8 layer, and the lattice constant is 250 nm. A periodic array of such cuboid-shaped nanoposts was simulated to find the transmission phases, which are plotted in Fig. 3B (see *Materials and Methods* for simulation details and *SI Appendix, Fig. S3B* for transmission powers). The diamond phase masks shown in Fig. 2D are sampled at 4 points with a 250-nm period, and the corresponding nanoposts are shown in Fig. 3B with black circles (see *SI Appendix, Fig. S3A* for the sampling points). The input

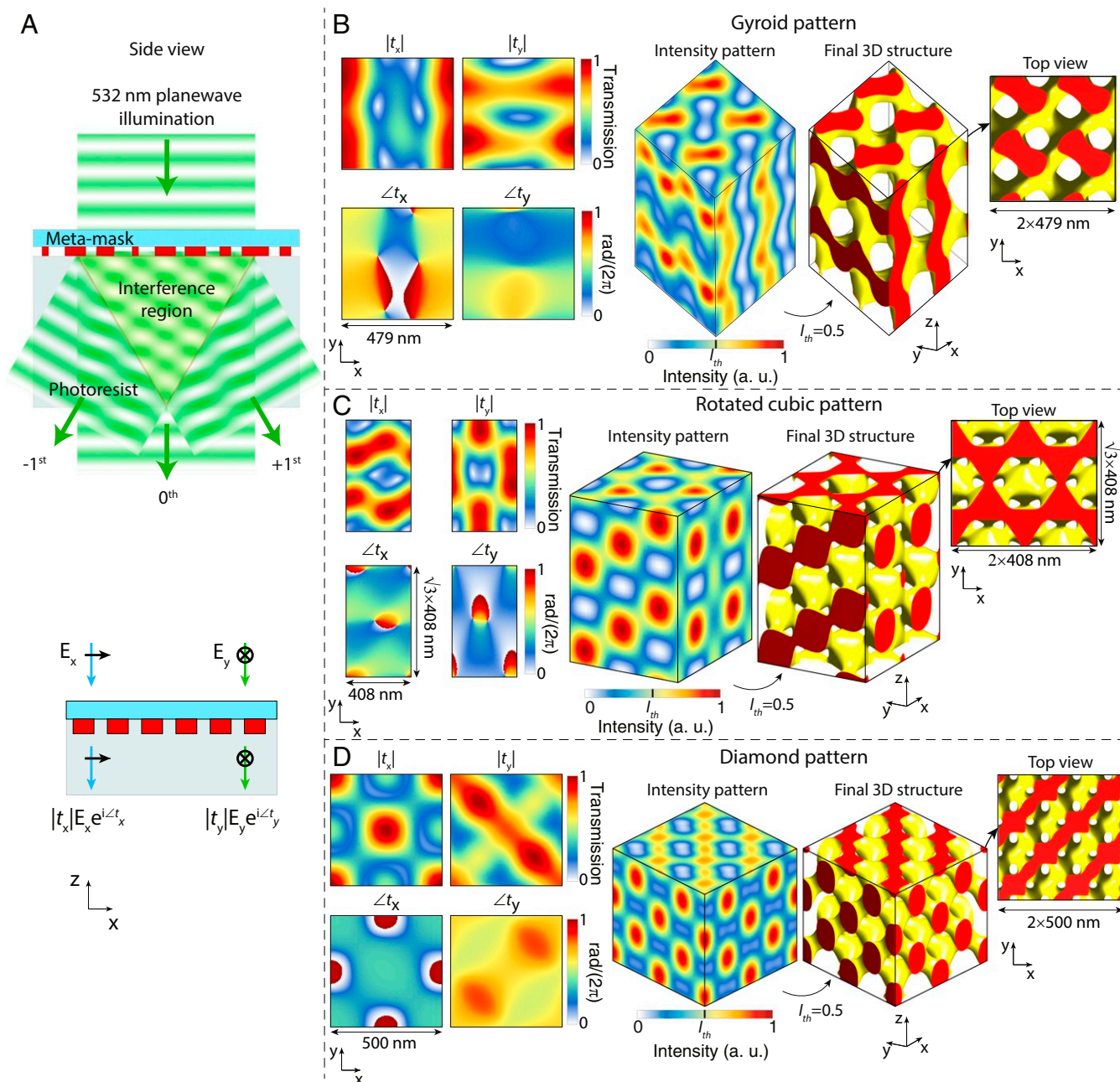


Fig. 2. Design of metamasks for generating desired 3D periodic patterns through interference. (A, Top) Schematic illustration of a metamask generating specific diffraction orders with designed complex coefficients to make a desired 3D pattern in the photoresist. (A, Bottom) Schematic of a metamask with amplitude, polarization, and phase control to make a desired 3D pattern. (B–D) x- and y-polarized transmission amplitudes and phases of different metamasks designed to create the gyroid, rotated cubic, and diamond patterns in the photoresist. The input light is assumed to be linearly polarized with $|E_x|/|E_y| = 0.85$, $|E_x|/|E_y| = 0.97$, and $|E_x|/|E_y| = 1$ for the 3 different patterns, respectively. (B–D, Left) Transmission amplitude and phases of the designed metamasks. (B–D, Center) generated 3D intensity patterns in the sensitized SU-8 photoresist under 532-nm laser illumination. (B–D, Right) Bird’s-eye view and top view of the expected 3D structures formed in the negative photoresist (sensitized SU-8) assuming a specific intensity threshold. Here, it is assumed that the regions with intensity values above 0.5 will be polymerized in the resist, and areas below this level are developed.

polarization is chosen such that $|E_x|/|E_y|$ is equal to $\langle |t_x| \rangle / \langle |t_y| \rangle$, where $\langle \cdot \rangle$ denotes averaging over a unit cell area. The full-wave simulated 3D intensity distribution and the corresponding periodic 3D structure are shown in Fig. 3C for this initial design. The fitness factor of this initial design is 84% and the total simulated transmission efficiency is 74% (see *Materials and Methods* for full-wave simulation details and [SI Appendix, Fig. S4A](#) for the phase and amplitude masks). To improve the degree of similarity of the achieved and desired

structures, we used this design as a starting point and further optimized the nanoposts' widths through a global optimization method. Considering the diagonal symmetry of the diamond metamask, the optimization parameters were reduced to 4 values (widths of the 2 different nanoposts). The optimized values are shown in Fig. 3B with black stars. The full-wave simulated 3D intensity profile and the resulting structure are shown in Fig. 3D in a volume equal to $2 \times 2 \times 2$ periods (see *SI Appendix, Fig. S4B* for the corresponding phase and

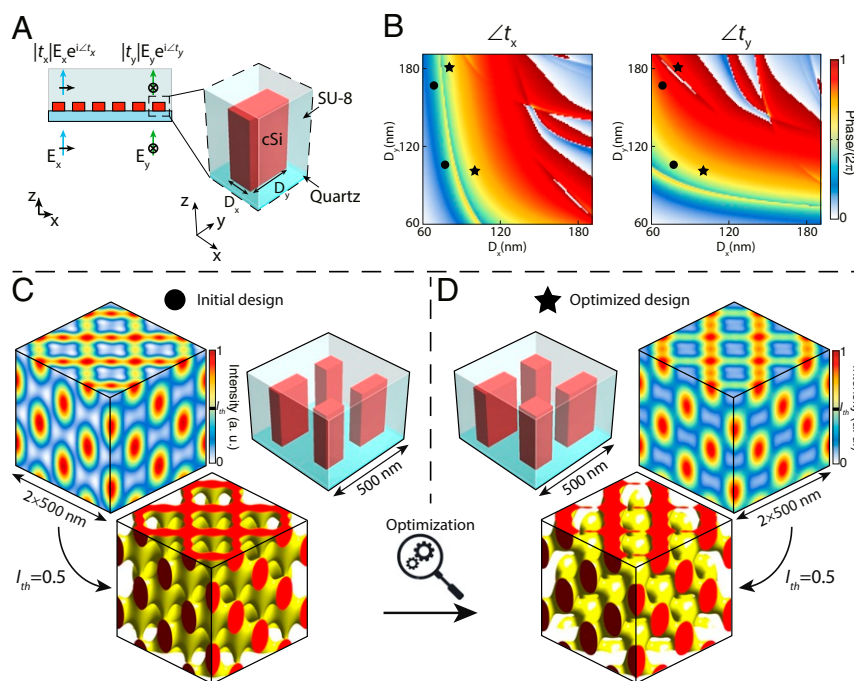


Fig. 3. Realization of the diamond pattern metamask with nanoposts. (A) Schematic drawing of different views of a uniform array of rectangular cross-section cSi nanoposts arranged in a square lattice resting on a quartz substrate and covered by an SU-8 layer. Tuning the in-plane dimensions of nanoposts, D_x and D_y , allows for independent control of the transmission phases of x- and y-polarized light at 532 nm. (B) Transmission phases of the x- and y-polarized light at 532 nm for the uniform array shown in A, as functions of the nanopost widths. The nanopost's height is 291 nm and the lattice constant is 250 nm. (C) The initial diamond metamask is designed through sampling the phase diagrams shown in Fig. 2D at 4 points. The corresponding nanopost dimensions are shown in B with black circles. The full-wave simulated 3D intensity pattern and the corresponding 3D structure demonstrate an 84% similarity compared to the target diamond pattern. (D) The nanopost dimensions are further optimized to realize a 90% similarity with the target diamond pattern. The optimized nanopost dimensions are shown in B with black stars. All simulations are performed at the wavelength of 532 nm. cSi: crystalline silicon. See *Materials and Methods* for simulation details.

amplitude masks). The fitness factor of the final optimized structure is 90% and the total simulated transmission efficiency is 82%. It is worth noting that the optimized metamask solution is not unique and various initial points or optimization techniques can result in different optimized designs. Details of the simulation and optimization steps are discussed in *Materials and Methods*.

The metamask is fabricated using standard nanofabrication techniques (see *Materials and Methods* for fabrication details). Fig. 4A, *Top* shows an optical image of the final fabricated device. A scanning electron micrograph of a part of the fabricated metamask before being capped with the SU-8 protecting layer is shown in Fig. 4A, *Bottom*.

To characterize the fabricated metamask we used a confocal microscopy setup with an oil immersion objective lens that captures all of the excited diffraction orders. The sample was illuminated by a 514-nm laser beam, which was the closest available laser line to 532 nm in the microscopy setup. The optical intensity distribution was captured in multiple parallel planes with ~ 45 -nm depth steps. Fig. 4B, *Right* shows the measured intensity profiles at 2 sample cross-sections (xy and xz planes as schematically shown in Fig. 4B). See *Materials and Methods* for details of the measurement procedure, and see *SI Appendix, Fig. S5* for measurement results over a larger area. The measured intensity profiles are in good agreement with the simulated results (simulated with the same illumination wavelength of 514 nm) as shown in Fig. 4B, *Left*. We attribute nonuniformities and small drifts in the z stack to sample vibrations and sample mount tilt angles.

The metamask-assisted 3D fabrication platform enables a fast, large-scale, and robust system for realizing exotic 3D structures. The realized 3D structures with nanoscale resolution could have

properties with great potential. For example, the gyroid, spiral, and diamond lattices show interesting optical properties (like optical chirality and photonic band structures) (46–48). Also, triply periodic gyroid, diamond, and cubic surfaces that have superior mechanical properties can be fabricated (49, 50) using the developed technique.

In this paper, we have focused on the generation of 3D lattices with wavelength-scale periodicities as we envision that the developed techniques will be mostly influential in this area. Nevertheless, the same concept using similar or different design methods can be extended to aperiodic 3D structures with the use of aperiodic metasurface masks (51). Specifically, one can think of these aperiodic metasurface masks as an extension of the superpixels used in the design of the periodic 3D lattices. Aside from 3D printing purposes, such aperiodic 3D patterns would expand the applications of this platform to other areas of science and technology like particle trapping, 3D structured light illumination, holography, optical microscopy, etc. Moreover, it is worth noting that high diffraction efficiencies provided by the metamasks result in high-contrast well-defined 3D structures in the photoresist even under fast single-photon lithography. Therefore, the use of metamask-assisted platforms could eliminate the limited intensity contrast issue faced in single-photon lithography that has previously been addressed through multiphoton lithography (52, 53). Furthermore, here we showcased the capability of this platform through a single-layer metasurface, while cascaded metasurface layers could also be designed to provide full and precise control over the complex coefficients of the 2 orthogonal polarization diffraction orders or provide additional control over the degrees of freedom like wavelength or illumination angle.

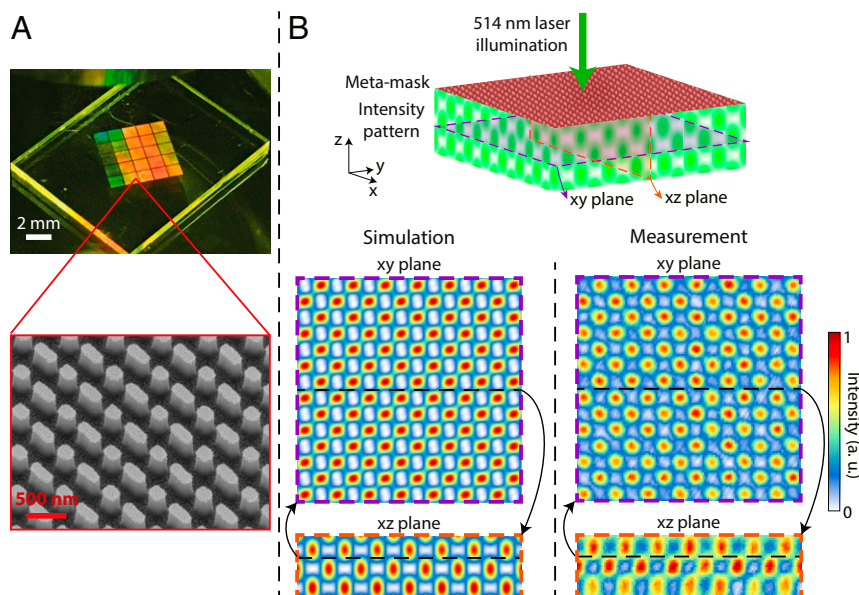


Fig. 4. Experimental characterization of the diamond metamask. (A, Top) Optical image of the fabricated optimized diamond metamask. A 5×5 array of masks is fabricated and shown on top. (A, Bottom) Scanning electron microscope image of a portion of the mask before spin coating the SU-8 layer. (B) The metamask is characterized under 514-nm laser illumination using a confocal microscopy setup (514-nm laser was the closest available laser line to 532 nm in the confocal microscopy setup). Two measured cross-sections of the captured 3D intensity pattern (Right) are in good agreement with the simulated results (Left).

In conclusion, here we introduce the concept of metamask-assisted interference lithography, which could provide a fast and robust technique for fabrication of exotic 3D periodic patterns at large scales. We demonstrated the versatility of this platform through designing different exotic 3D patterns like the gyroid, rotated cubic, and diamond. Moreover, as a proof of concept, we experimentally demonstrate the diamond pattern through design and fabrication of the metamask. Besides large-scale interference lithography with nanoscale resolution, the presented concept can be used to generate complex 3-dimensional light fields for various applications including structured light illumination, microscopy, particle trapping, and holography.

Materials and Methods

Simulation and Optimization Procedure. To find the optimized complex coefficients of different diffraction orders and the input polarization for generating the target 3D periodic pattern, we used a global particle swarm optimization method. For the diamond and rotated cubic structures, we forced the coefficients of unwanted diffraction orders to be zero. The target 3D patterns were defined with voxel sizes of $\sim 10 \text{ nm}^3$ and $\sim 13 \text{ nm}^3$ for the rectangular (gyroid and diamond) and triangular (rotated cubic) lattices, respectively.

To find the transmission powers and phases of a uniform array of nanoposts under x - and y -polarized illumination, the rigorous coupled-wave analysis (RCWA) technique was used (54). x - and y -polarized incident plane waves at 532 nm wavelength were used as the excitation, and the transmission powers and phases of the x - and y -polarized transmitted waves were extracted. The subwavelength 250-nm lattice constant in the SU-8 propagating medium results in the excitation of only the zeroth-order diffracted light. The cSi layer was assumed to be 291 nm thick. Refractive indexes at 532-nm wavelength were assumed as follows: cSi, $4.136 - 1j0.01027$; SU-8, 1.595; and quartz, 1.4607. The nanopost in-plane dimensions (D_x and D_y) were swept such that the minimum feature size and the gap size remain larger than 60 nm for relieving fabrication constraints.

We used the finite-difference time-domain method (Lumerical) for simulating the metamasks realized with cSi nanoposts. The electric fields were extracted on an xy plane $\sim 20 \text{ nm}$ above the nanoposts. We used the plane-wave expansion (PWE) technique (55) to generate the 3D intensity profiles and the 3D structures.

To optimize the nanoposts' in-plane dimensions for the diamond metamask, we used a global particle swarm optimization method with the fitness factor (FF) target function. To find the 3D structure, we used the same Lumerical simulation package with the PEW technique.

Sample Fabrication. To define the pattern in cSi on quartz wafers, a Vistec EBPG5200 e-beam lithography system and an $\sim 300\text{-nm}$ -thick layer of ZEP-520A positive electron-beam resist were used (spin coated at 5,000 rpm for 1 min). The pattern was developed in the resist developer (ZED-N50 from Zeon Chemicals) for 3 min. The pattern was then transferred into an $\sim 50\text{-nm}$ -thick deposited Al_2O_3 layer, by a lift-off process. The patterned Al_2O_3 hard mask was then used to dry etch the cSi layer in a mixture of SF_6 and C_4F_8 plasma. Finally, the Al_2O_3 mask was removed in a 1:1 solution of ammonium hydroxide and hydrogen peroxide at 80°C . Finally, a $2\text{-}\mu\text{m}$ -thick layer of SU-8 protecting layer was spin coated on the metamask.

Measurement Procedure. The diamond metamask was measured using a confocal microscopy setup (Zeiss LSM 710). A $100\times$ oil immersion objective lens (alpha Plan-Apochromat Oil DIC M27, numerical aperture [NA] = 1.46) was used to capture all of the excited diffraction orders, as the diamond mask has NA ~ 1.45 at 514-nm wavelength. We used Zeiss Immersol 518 F with a refractive index of 1.518, which was the closest allowed oil in the microscopy setup to the refractive index of SU-8 (1.595). We captured 3D image stacks with in-plane pixel sizes of $\sim 28 \text{ nm}^2$ and in-depth pixel sizes of $\sim 45 \text{ nm}$. We captured in-plane images as large as $15 \mu\text{m}^2$, shown in SI Appendix, Fig. S5. We should note that the resolution of the system is set by the objective lens and is $\sim 176 \text{ nm}$ and $\sim 482 \text{ nm}$ in-plane and in-depth, respectively.

ACKNOWLEDGMENTS. This work was supported by the Department of Energy (DOE) "Light-Material Interactions in Energy Conversion" Energy Frontier Research Center funded by the US DOE, Office of Science, Office of Basic Energy Sciences under Grant DE-SC0001293. The device nanofabrication was performed at the Kavli Nanoscience Institute at California Institute of Technology (Caltech). Confocal imaging was performed at the Caltech Biological Imaging Facility with the support of the Caltech Beckman Institute and the Arnold and Mabel Beckman Foundation; we thank Dr. Andres Collazo for his help in the confocal microscopy. We thank Prof. Julia Greer, Dr. Travis Blake, Prof. Amir Arbabi, and Daniel Bacon-Brown for fruitful discussion. We also thank Sana Kamali for the artistic renders.

1. J. R. Tumbleston *et al.*, Continuous liquid interface production of 3d objects. *Science* **347**, 1349–1352 (2015).
2. J. B. Reeves, R. K. Jayne, L. Barrett, A. E. White, D. J. Bishop, Fabrication of multi-material 3d structures by the integration of direct laser writing and MEMS stencil patterning. *Nanoscale* **11**, 3261–3267 (2019).
3. T. A. Schaedler *et al.*, Ultralight metallic microlattices. *Science* **334**, 962–965 (2011).
4. D. W. Yee, M. D. Schulz, R. H. Grubbs, J. R. Greer, Functionalized 3d architected materials via thiol-michael addition and two-photon lithography. *Adv. Mater.* **29**, 1605293 (2017).
5. H. Ning *et al.*, Holographic patterning of high-performance on-chip 3D lithium-ion microbatteries. *Proc. Natl. Acad. Sci. U.S.A.* **112**, 6573–6578 (2015).
6. S. V. Murphy, A. Atala, 3d bioprinting of tissues and organs. *Nat. Biotechnol.* **32**, 773–785 (2014).
7. T.-S. Wei, B. Y. Ahn, J. Grotto, J. A. Lewis, 3d printing of customized li-ion batteries with thick electrodes. *Adv. Mater.* **30**, 1703027 (2018).
8. K. A. Arpin *et al.*, Multidimensional architectures for functional optical devices. *Adv. Mater.* **22**, 1084–1101 (2010).
9. H. Gong, B. P. Bickham, A. T. Woolley, G. P. Nordin, Custom 3d printer and resin for $18\ \mu\text{m} \times 20\ \mu\text{m}$ microfluidic flow channels. *Lab Chip* **17**, 2899–2909 (2017).
10. Y. A. Vlasov, X.-Z. Bo, J. C. Sturm, D. J. Norris, On-chip natural assembly of silicon photonic bandgap crystals. *Nature* **414**, 289–293 (2001).
11. S. Vignolini *et al.*, A 3d optical metamaterial made by self-assembly. *Adv. Mater.* **24**, OP23–OP27 (2012).
12. M. Campbell, D. N. Sharp, M. T. Harrison, R. G. Denning, A. J. Turberfield, Fabrication of photonic crystals for the visible spectrum by holographic lithography. *Nature* **404**, 53–56 (2000).
13. J.-H. Jang *et al.*, 3d micro-and nanostructures via interference lithography. *Adv. Funct. Mater.* **17**, 3027–3041 (2007).
14. S.-K. Lee, S.-G. Park, J. H. Moon, S.-M. Yang, Holographic fabrication of photonic nanostructures for optofluidic integration. *Lab Chip* **8**, 388–391 (2008).
15. I. Wathuthanthri, Y. Liu, K. Du, W. Xu, C.-H. Choi, Simple holographic patterning for high-aspect-ratio three-dimensional nanostructures with large coverage area. *Adv. Funct. Mater.* **23**, 608–618 (2013).
16. D. A. Bacon-Brown, P. V. Braun, Tunable antireflection coating to remove index-matching requirement for interference lithography. *Adv. Opt. Mater.* **6**, 1701049 (2018).
17. B. E. Kelly *et al.*, Volumetric additive manufacturing via tomographic reconstruction. *Science* **363**, 1075–1079 (2019).
18. S. Matthias, F. Müller, Asymmetric pores in a silicon membrane acting as massively parallel Brownian ratchets. *Nature* **424**, 53–57 (2003).
19. M. Vaezi, H. Seitz, S. Yang, A review on 3d micro-additive manufacturing technologies. *Int. J. Adv. Manuf. Technol.* **67**, 1721–1754 (2013).
20. F. P. W. Melchels, J. Feijen, D. W. Grijpma, A review on stereolithography and its applications in biomedical engineering. *Biomaterials* **31**, 6121–6130 (2010).
21. J. Mueller, J. R. Raney, K. Shea, J. A. Lewis, Architected lattices with high stiffness and toughness via multicore-shell 3d printing. *Adv. Mater.* **30**, 1705001 (2018).
22. S. Jeon *et al.*, Fabricating complex three-dimensional nanostructures with high-resolution conformable phase masks. *Proc. Natl. Acad. Sci. U.S.A.* **101**, 12428–12433 (2004).
23. S. Jeon, Y.-S. Nam, D. J.-L. Shir, J. A. Rogers, A. Hamza, Three dimensional nanoporous density graded materials formed by optical exposures through conformable phase masks. *Appl. Phys. Lett.* **89**, 253101 (2006).
24. S. M. Kamali, E. Arbabi, A. Arbabi, A. Faraon, A review of dielectric optical metasurfaces for wavefront control. *Nanophotonics* **7**, 1041–1068 (2018).
25. A. V. Kildishev, A. Boltasseva, V. M. Shalae, Planar photonics with metasurfaces. *Science* **339**, 1232009 (2013).
26. P. Lalanne, P. Chavel, Metalenses at visible wavelengths: Past, present, perspectives. *Laser Photon. Rev.* **11**, 1600295 (2017).
27. P. Qiao, W. Yang, C. J. Chang-Hasnain, Recent advances in high-contrast meta-structures, metasurfaces, and photonic crystals. *Adv. Opt. Photon.* **10**, 180–245 (2018).
28. H.-H. Hsiao, C. H. Chu, D. P. Tsai, Fundamentals and applications of metasurfaces. *Small Methods* **1**, 1600064 (2017).
29. A. Arbabi *et al.*, Miniature optical planar camera based on a wide-angle meta-surface doublet corrected for monochromatic aberrations. *Nat. Commun.* **7**, 13682 (2016).
30. Y. Horie, A. Arbabi, E. Arbabi, S. M. Kamali, A. Faraon, Wide bandwidth and high resolution planar filter array based on DBR-metasurface-DBR structures. *Opt. Express* **24**, 11677–11682 (2016).
31. E. Arbabi, A. Arbabi, S. M. Kamali, Y. Horie, A. Faraon, Controlling the sign of chromatic dispersion in diffractive optics with dielectric metasurfaces. *Optica* **4**, 625–632 (2017).
32. A. Arbabi, E. Arbabi, Y. Horie, S. M. Kamali, A. Faraon, Planar metasurface retroreflector. *Nat. Photon.* **11**, 415–420 (2017).
33. E. Arbabi *et al.*, MEMS-tunable dielectric metasurface lens. *Nat. Commun.* **9**, 812 (2018).
34. M. L. Solomon, J. Hu, M. Lawrence, A. García-Etxarri, J. A. Dionne, Enantiospecific optical enhancement of chiral sensing and separation with dielectric metasurfaces. *ACS Photon.* **6**, 43–49 (2018).
35. C.-H. Liu *et al.*, Ultrathin van der Waals metalenses. *Nano Lett.* **18**, 6961–6966 (2018).
36. M. Decker *et al.*, Imaging performance of polarization-insensitive metalenses. *ACS Photon.* **6**, 1493–1499 (2019).
37. A. L. Holsteen, D. Lin, I. Kauvar, G. Wetzstein, M. L. Brongersma, A light-field metasurface for high-resolution single-particle tracking. *Nano Lett.* **19**, 2267–2271 (2019).
38. S. M. Kamali, A. Arbabi, E. Arbabi, Y. Horie, A. Faraon, Decoupling optical function and geometrical form using conformal flexible dielectric metasurfaces. *Nat. Commun.* **7**, 11618 (2016).
39. A. Arbabi, Y. Horie, M. Bagheri, A. Faraon, Dielectric metasurfaces for complete control of phase and polarization with subwavelength spatial resolution and high transmission. *Nat. Nanotechnol.* **10**, 937–943 (2015).
40. S. M. Kamali, E. Arbabi, A. Arbabi, Y. Horie, A. Faraon, Highly tunable elastic dielectric metasurface lenses. *Laser Photon. Rev.* **10**, 1002–1008 (2016).
41. A. Leitis *et al.*, Angle-multiplexed all-dielectric metasurfaces for broadband molecular fingerprint retrieval. *Sci. Adv.* **5**, eaaw2871 (2019).
42. S. M. Kamali *et al.*, Angle-multiplexed metasurfaces: Encoding independent wavefronts in a single metasurface under different illumination angles. *Phys. Rev. X* **7**, 041056 (2017).
43. A. Howes, W. Wang, I. Kravchenko, J. Valentine, Dynamic transmission control based on all-dielectric Huygens metasurfaces. *Optica* **5**, 787–792 (2018).
44. L. Z. Cai, X. L. Yang, Y. R. Wang, All fourteen Bravais lattices can be formed by interference of four noncoplanar beams. *Opt. Lett.* **27**, 900–902 (2002).
45. S. Yang *et al.*, Creating periodic three-dimensional structures by multibeam interference of visible laser. *Chem. Mater.* **14**, 2831–2833 (2002).
46. L. Wu, W. Zhang, D. Zhang, Engineering gyroid-structured functional materials via templates discovered in nature and in the lab. *Small* **11**, 5004–5022 (2015).
47. J. K. Gansel *et al.*, Gold helix photonic metamaterial as broadband circular polarizer. *Science* **325**, 1513–1515 (2009).
48. Y. K. Pang *et al.*, Chiral microstructures (spirals) fabrication by holographic lithography. *Opt. Express* **13**, 7615–7620 (2005).
49. O. Al-Ketan *et al.*, Microarchitected stretching-dominated mechanical metamaterials with minimal surface topologies. *Adv. Eng. Mater.* **20**, 1800029 (2018).
50. S. C. Han, J. W. Lee, K. Kang, A new type of low density material: Shellular. *Adv. Mater.* **27**, 5506–5511 (2015).
51. S. M. Kamali, E. Arbabi, A. Faraon, “Metasurface-assisted 3d beam shaping.” US Patent App. 16/209,788 (2019).
52. S. Jeon, V. Malyarchuk, J. A. Rogers, G. P. Wiederrecht, Fabricating three dimensional nanostructures using two photon lithography in a single exposure step. *Opt. Express* **14**, 2300–2308 (2006).
53. D. Shir *et al.*, Three dimensional silicon photonic crystals fabricated by two photon phase mask lithography. *Appl. Phys. Lett.* **94**, 011101 (2009).
54. V. Liu, S. Fan, S4: A free electromagnetic solver for layered periodic structures. *Comput. Phys. Commun.* **183**, 2233–2244 (2012).
55. M. Born, E. Wolf, A. B. Bhatia, *Principles of Optics: Electromagnetic Theory of Propagation, Interference and Diffraction of Light* (Cambridge University Press, 1999).